NJC

Accepted Manuscript

This is an *Accepted Manuscript*, which has been through the Royal Society of Chemistry peer review process and has been accepted for publication.

Accepted Manuscripts are published online shortly after acceptance, before technical editing, formatting and proof reading. Using this free service, authors can make their results available to the community, in citable form, before we publish the edited article. We will replace this *Accepted Manuscript* with the edited and formatted *Advance Article* as soon as it is available.

You can find more information about *Accepted Manuscripts* in the Information for Authors.

Please note that technical editing may introduce minor changes to the text and/or graphics, which may alter content. The journal's standard Terms & Conditions and the Ethical guidelines still apply. In no event shall the Royal Society of Chemistry be held responsible for any errors or omissions in this *Accepted Manuscript* or any consequences arising from the use of any information it contains.

ROYAL SOCIETY OF CHEMISTRY

www.rsc.org/njc

NJC

ARTICLE

Electrospun porous hierarchical carbon nanofibers with tailored structures for supercapacitors and capacitive deionization

Received 00th January 20xx,
Accepted 00th January 20xx

DOI: 10.1039/x0xx00000x

www.rsc.org/

G. Wang, B. Q. Qian, Y. W. Wang, Q. Dong, F. Zhan, and J. S. Qiu

Hierarchical porous carbons, which contain micropores combined with mesopores and/or macropores, promote mass transport through the macropores/mesopores and increase the accessibility of smaller pores compared with single-sized porous carbons. However, current synthesis procedures cannot fabricate tailored hierarchical carbons with both freestanding structure and mesoporosity. In this work, electrospun porous hierarchical carbon nanofibers with a macro two-dimensional monolithic structure was successfully prepared through electrospinning combined with poly(vinylpyrrolidone) template method. The performance of these nanofibers as an electrode material for supercapacitors and the vertical flow-through capacitive deionization for desalination were studied to determine the structural characteristics of the macro two–dimensional monolithic material. This work provides a general approach for preparing carbons with controlled hierarchical pore structures and new insights into the advanced utilization of carbon materials.

Introduction

Cost-effective deionization of brackish water is more energy-efficient than the widely used reverse osmosis and evaporation and thus suitable to resolve the growing freshwater crisis. Capacitive deionization (CDI), which is based on the principle of electric double layer capacitors, is a promising technology for desalination of saline water because of its low power requirements[1-8]. However, the lack of a suitable electrode material and configuration has hindered the industrial applications of CDI[9].

Nanoporous carbon materials with a porous hierarchical structure have been developed and utilized for CDI technology; these materials include hierarchical activated carbon nanofibers[10, 11],hierarchical ordered mesoporous carbon[12], graphene/carbon nanotube hybrid sponges[13, 14],and graphene-coated mesoporous carbon spheres[15,16]. Hierarchical structures with a balanced ratio of macropores (60–100 nm), mesopores (2–50 nm), and micropores (<2 nm) significantly influence the transport of salt ions and thus enhance the CDI performance. However, the configuration of future CDI devices must be improved to enhance their performance for desalination. Suss *et al*.[3, 17] designed an architecture, in which the feed flows directly through electrodes along the primary electric field direction; this process is known as flow-through electrode capacitive desalination. The removal efficiency of a cell with the flow-through CDI architecture is4 to 10 times higher than that of a typical flow-by cell. Moreover, CDI utilizing the flow electrode (FCDI) is an innovative design for seawater desalination[18]. The FCDI cell exhibits excellent removal efficiency (95%) and high electrosorption capacity ($25 mg \cdot g^{-1}$). Yury *et al*.[19] also proposed an FCDI architecture that facilitates desalination without using ion exchange membranes or feed stream between electrodes. This architecture is suitable for compact and low-resistance systems, which use carbon slurry.

Electrospun porous carbon nanofiber (CNF) has attracted much attention because of its interesting properties, such as freestanding structure, high electrical conductivity, and large surface area[20, 21].CNF and its hybrids are used for various applications, including electrochemical capacitors[22], environmental protection[23], CDI[24], and catalyst supports[25]. CNF is typically microporous with a large surface area and good conductivity. However, the microporosity of CNF is unnecessary and undesirable for most applications because micropores tend to act as deep trap sites and enhance inner-pore ion transport resistance and diffusion distance.

Numerous efforts have been devoted to produce electrospun porous hierarchical carbon nanofiber (PCNF). The porous hierarchical texture of PCNF comprises mesopores and micropores; in this structure, micropores enhance the electric double layer capacitance and mesopores provide low-resistance pathways for ions though porous fibers[26]. To add a template to this structure, a polymer or other additive precursors are included in the electrospinning precursor solution, thereby producing mesopores after carbonization.

State Key Lab of Fine Chemicals,Liaoning Key Lab for Energy Materials and ChemicalEngineering, PSU-DUT Joint Center for Energy Research, Dalian University of Technology, Dalian 116024, P. R. China. E-mail:jqiu@dlut.edu.cn (J. S. Qiu)

Binary polymer solution containing polyacrylonitrile (PAN) and poly(methyl methacrylate) (PMMA) can be electrospun. PMMA is completely eliminated during carbonization to synthesize PCNF with hierarchical structures because these polymers exhibit different thermal properties[27-29]. Mesopore volume (V_{meso}) can be controlled by changing the PAN/PMMA ratio; V_{meso} increases from 0.18 $cm^3 \cdot g^{-1}$ for 9/1 ratio to 0.47 $cm^3 \cdot g^{-1}$ for the 5/5 ratio, but the micropore volume (V_{micro}) is constant at 0.34 $cm^3 \cdot g^{-1}$. Accordingly, PCNF exhibits a salt removal efficiency of 90% in CDI applications and a specific capacitance of 237 $F \cdot g^{-1}$.

Dimethyl sulfone ($DMSO_2$) is also used as a pore-forming agent to fabricate PAN/$DMSO_2$ nanofibers by electrospinning the PAN/$DMSO_2$ mixture in *N*,*N*-dimethyl formamide solution. Based on the evaporation properties of $DMSO_2$ at moderate temperatures, uniform meso-/micropores can be formed in the nanofibers during preoxidation of PAN without requiring additional treatments. Furthermore, when the PAN/$DMSO_2$ ratio in the precursor solution changes from 3/2 to 2/3, carbon nanofibers exhibit S_{BET} from 462 $m^2 \cdot g^{-1}$ to 212 $m^2 \cdot g^{-1}$ and mesoporous volume ratio V_{meso}/V_T from 8.3% to 42.4%[30].The electrochemical properties and desalination amount of PCNF electrodes are greatly improved compared with those of pure PAN-based CNF electrodes because of the suitable micro-/meso structure contribution.

In this paper, we presented a simple method used to synthesize freestanding PCNF with tailored pore structures by mixing poly(vinylpyrrolidone) (PVP) into PAN. PVP was dissolved from the as-spun fibers at 100 °C under hydrothermal condition. The resultant PAN nanofibers were stabilized and then carbonized at 800 °C. Changes in the PAN/PVP ratio in the precursor solution generated carbon nanofibers with porous hierarchical structures[31]. The fabricated nanofibers were used as an electrode material in supercapacitors without binders or conductive additives and showed high specific capacitance of more than 100 $F \cdot g^{-1}$ at 50 $A \cdot g^{-1}$ and excellent cyclic stability for 10000 cycles. As an electrode material in custom-built FCDI cell, novel PCNF, which includes micro-scale pores between interwoven fibers and sub-10 nm pores, exhibited high current efficiency and electrosorption capacity.

Experimental

Preparation of PCNF

Precursor solutions were prepared by dissolving polyvinylpyrrolidone (PVP; Mw = 1300000, Aldrich)and polyacrylonitrile (PAN; Mw = 150000, Aldrich)with dimethylformamide (DMF) under magnetic stirring at 60 °Cfor6 h. In this work, a simple yet effective process for preparing PCNF was introduced, that is, non-woven supports for the overall structure were used to prepare monolithic porous carbon nanofibers (PCNF) with a high mesoporous rate during removal of the PVP template with hot water (Fig. 1a). Four samples were prepared at PVP/PAN/DMF weight ratios of 0/0.8/9, 0.2/0.8/9, 0.5/0.8/9, and 0.8/0.8/9. The obtained homogenous solutions were then aspirated into a 10 mL syringe with a capillary tip (0.8 mm in diameter) connected to a high voltage power source. The collector is a rotating metal drum wrapped with aluminum foil and set 15 cm away from the syringe tip. Each sample was subjected to a normalized electrospinning process with 22 kV high voltage and 2 $mL \cdot h^{-1}$ feeding speed. The obtained electrospun nanofibers (NFs) were split carefully from aluminum foil and named as NF0, NF1, NF2, and NF3, which correspond to PVP/PAN weight ratios of 0/0.8, 0.2/0.8,0.5/0.8, and 0.8/0.8, respectively.

The as-collectedelectrospun NFs were cut into 6 cm ×6 cm pieces(Fig. 1b) and then transferred into a 100 mL Teflon stainless steel autoclave. Each piece was clamped by PP nonwoven fabrics before adding deionized water to stabilize the monolithic cloth structure under drastic hydrothermal conditions. The hydrothermal treatment was conducted at 120 °C for 24 h to remove PVP templates. The extracted NFs were washed with DI water and dehydrated by vacuum filtration for several times to remove residual PVP templates. PVP-removed porous nanofibers (PNFs, Fig. 1c) were obtained after freeze drying and named as PNF0, PNF1, PNF2, and PNF3. The obtained PNFs were stabilized in air at 280 °C for 1 h with a heating rate of 1 $°C \cdot min^{-1}$ and then carbonized in N_2 at 800 °C for 0.5 h, followed by activation in CO_2 with a heating rate of 5 $°C \cdot min^{-1}$ for 0.5 h. The as-obtained PCNFs (Fig. 1d) were named PCNF0, PCNF1, PCNF2, and PCNF3. Fig. 1e shows the alterations in the size of PNF and PCNF obtained according to different PVP/PAN proportions. The sizes of the obtained PCNF products were successively reduced with increasing PVP content.

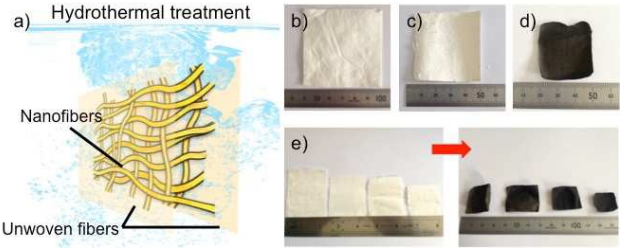

Fig. 1 (a) Schematic of modified PVP–template method for preparation of monolithic PCNFs; and (b–e) digital images of NF, PNF, CNF, and PCNF, respectively.

Characterization

Morphology was characterized by field emission scanning electron microscopy (FE-SEM; FEI, Nova 450). Variations in the composition of NFs and PNFs were determined by thermogravimetric analysis (TGA; NETZSCH, STA449). Brunauer–Emmett–Teller (BET) surface area and pore size distribution (PSD) were evaluated with nitrogen adsorption isotherm (Micrometrics, ASAP2020). The samples were degassed at 250 °C for 5 h under vacuum before measurements. Total pore volume was estimated from the

amount of nitrogen adsorbed at $P/P_0 = 1$. Micropore volume and size were calculated with the Dubinin–Radushkevich (DR) equation and Horvath–Kawazoe (HK) method, respectively. PSD was calculated by density functional theory (DFT)[32].

Electrochemical and CDI measurements

The electrochemical performance of PCNFs in terms of cyclic voltammetry (CV), galvanostatic charge–discharge (GC), and electrochemical impedance spectroscopy (EIS) was measured on an electrochemical station (Biologic, VMP3). A three-electrode configuration was employed with 6 M KOH as aqueous electrolyte, where the Hg/HgO electrode was set as the reference and the Pt electrode as the counter. Electrochemical stabilization was studied with GC from −0.1 V to −0.9 V (*vs.* Hg/HgO) at a constant current density of 5 $A \cdot g^{-1}$ with a Land Battery workstation to investigate the potential of PCNFs for supercapacitors.

CDI experiments were conducted with a typical batch-mode set-up. As shown in Fig. 2a, the middle of the graphite current collectors in contact with electrodes at two sides were punched to form a channel for flowing of salt solution. The middle part of the two pieces of monolithic carbon nanofiber electrodes (mass of approximately 55 mg) was separated with non-woven structure through direct contact with the current collectors to form a voltage channel. The middle part was then clamped in the middle of the two-sided current collectors. Raw feed water flows from one side of direction vertical to the electrode and then from the other side to form a vertical flow-through CDI structure(Fig. 2b). Meanwhile, the hollow part of the rubber cushion was cushioned between the two electrode plates. This part must also be of the same size with graphite to ensure that the fluid does not directly flow through the CDI module from the surrounding gaps and ensure that the fluid passes through the electrode pieces. Figs. 2c and 2d show the comparison images of the vertical flow-through CDI module and the parallel flow-by CDI module, respectively.

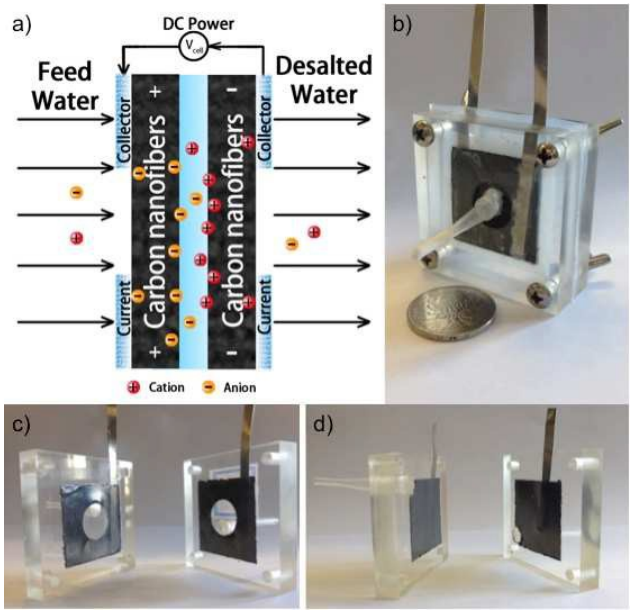

Fig.2(a) Schematic of the flow-through CDI module; (b, c) digital images of the flow-through CDI module; and (d) digital image of the flow-by CDI module.

Results and discussion

TGA was conducted to analyze the components of the prepared NF and PNF and verify whether the PVP template solvent is successfully and completely removed during the hydrothermal process. In N_2atmosphere, the temperature was increased from room temperature to 800°C at 10°C min^{-1} to obtain the TGA curves of NF and PNF (Fig. 3). Solid lines in Fig. 3 show the TGA curves of NF1, NF2, and NF3. The curves show that the PVP content of the components increases with increasing PVP content in the electrospinning precursor solution. The PAN components start to decompose at approximately 300 °C, where as the PVP components start to decompose when the temperature was increased to approximately 360 °C. The TGA curves also show the prominent two-sectional ladder decomposition curves. The dotted lines represent the TGA curves of PNF1, PNF2, and PNF3, which were obtained during the removal of the PVP template solvent through a hydrothermal process. Weight loss of the PVP component in the NF curve basically disappears in the PNF curve, whereas that of the decomposed PAN component becomes almost equal. This finding indicates that the TGA curve is basically converted into a one-sectional decomposition curve. Therefore, most of the PVP template solvent in the blended nanofibers was possibly removed through the hydrothermal method. Despite the small amount of PVP residues, porous nanofibers with the highest amount of PAN component were obtained.

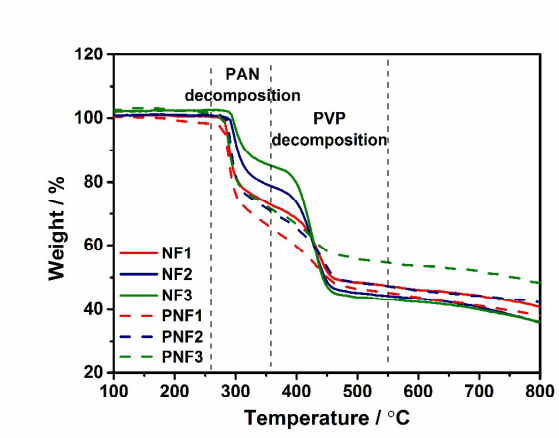

Fig.3 TGA analysis of porous nanofibers.

Field emission scanning electron microscopy(FE-SEM; FEI, Nova 450) analysis was performed to characterize the morphology of NF and PNF. Fig. 4 shows the FE-SEM micrographs and fiber diameter analysis for NF and PNF. In Figs. 4a–4c, NF showed superfine nano-level fiber structures. The diameters of the fibers basically comply with the normal distribution law, and the average diameter increases with increasing PVP content in the electrospinning precursor solution (NF1: 0.44 μm; NF2: 0.54 μm; and NF3: 0.87 μm). Increase in PVP content increases the viscosity and surface tension of the electrospinning precursor solution because PVP, with molecular weight higher than that of PAN, was used as the polymer precursor. This phenomenon results in increased diameter of the obtained electrospun fiber under the same electrospinning parameters. After the hydrothermal treatment, PVP components in the nanofibers were dissolved in water and removed. The obtained PNF is shown in Figs. 4d–4f. PNF obtained through process improvement shows folded and course surfaces and porous structures. However, after the PVP components of the fibers were removed, a certain degree of shrinkage occurs to maintain the macro-scale two-dimensional monolithic structure because of the domain limit function of non-woven support in the hydrothermal process; thus, the microporous structure in the FE-SEM images shrinks and shows densely distributed small-sized porous structures.

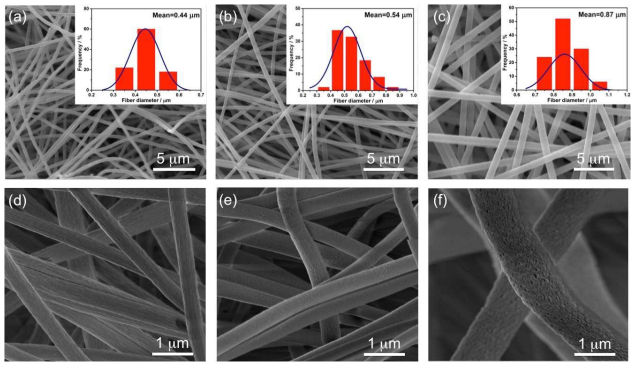

Fig.4 FE-SEM images of materials: (a) NF1; (b) NF2; (c) NF3; (d) PNF1; (e) PNF2; and (f) PNF3.

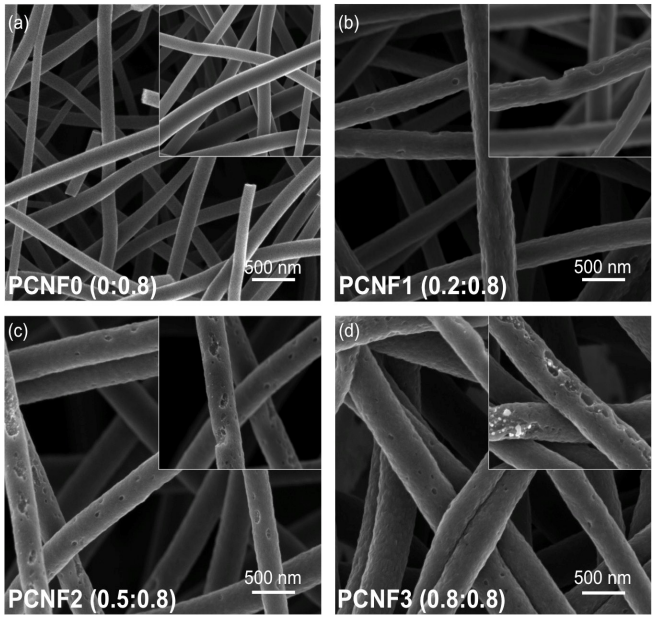

Fig.5 FE-SEM micrographs of materials: (a) CNFs; (b) PCNF1; (c) PCNF2; and (d) PCNF3.

Figs. 5a–5d represent the FE-SEM micrographs of CNF and PCNF electrodes obtained through carbonization and activation under the same magnification factor. The fibers of the CNF electrode show smooth surfaces, which are almost defect-free (Fig. 5a). By contrast, the fibers of the PCNF electrode exhibit prominent unsmooth coarse surfaces. Moreover, several pores with different sizes were observed. The obtained PCNF surface roughness prominently increases with increasing content of the PVP template solvent. The slight fold surface of PCNF1 gradually develops into a scattered hole surface of PCNF2 and then into the widely distributed dense holes of the fiber surface of PCNF3 (Figs. 5b–5d). Simultaneously, the comparison shows that the fiber diameter increases in the same manner as the nanofibers, which are not carbonized and activated, with increasing PVP content.

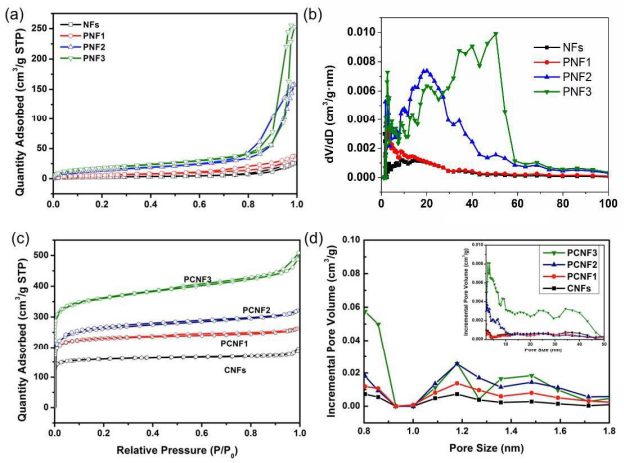

Fig. 6 (a, c) Nitrogen adsorption and desorption isotherms; and (b, d) PSD of the samples.

Fig. 6a shows the N_2 adsorption–desorption isotherms of PNFs and PCNF. According to the IUPAC category, all samples belong to category II non-porous or large porous isotherms; hence, PNFs have nearly no micropores. Moreover, the adsorption quantity gradually increases after the addition of PVP template solvent with increasing PVP/PAN portions. The hysteresis loop gradually becomes prominent when the relative pressure P/P_0 is within 0.8–1.0.Hence, increase in the specific surface area of porous fibers could be due to the contribution of mesopores or macropores, which were formed after removing the PVP template.

Mesoporous content increases with increasing PVP template solvent content. Fig. 6b shows the porous diameter distribution of NFs and PNFs within 0–100 nm. With the introduction of PVP template solvent, PNF possesses a nano-scale pore volume, which is higher than that of NFs. Moreover, PNFs are mainly distributed within a large mesoporous scale between 20 and 60 nm. Fig. 6c shows the N_2 adsorption–desorption isotherms of CNF and PCNF. All the isotherms typically belong to category I isotherms. Specifically, micropores play a dominant role in the pore structure of the material. CO_2 activation increases the micropore volume for the material and plays an active role in electrochemical and electro-adsorption applications. Similar to the trend in Fig. 6a, adsorption volume, which is based on the adsorption isotherms, evidently increases with increasing PVP template solvent, thereby increasing the specific surface area. At the highest portion of PVP/PAN in PCNF3,theadsorption isotherm has a prominent hysteresis loop relative to the other materials within the relative pressure P/P_0 scope between 0.8 and 1.0.Hence, mesopore content is high in this pore structure. The PSD patterns of CNFs and PCNF are shown in Fig. 6d.The distributions of the four electrode materials are basically identical when the micropore size is less than 2 nm. This result coincides with that in Fig. 6b because the micropores of the material are mainly derived from carbonization and activation under the same process conditions. However, within the mesoporous size range of 2–50 nm, the PSD of PCNF gradually improveswith increasingPVP/PAN proportion.Whenthe PVP addition is less in PCNF1, the difference fromCNFs is not prominent,whereasthe distribution content of PCNF2 within the mesoporous size range of2–10 nm is higher than those in CNFs and PCNF1. In particular, PSD within the large mesoporous size range of10–50 nm is higher than that of the three other materials, given the PCNF3 material with the highest proportion of PVP/PAN.

Table 1 Physicaladsorption characteristics and density.

Samples	BET ($m^2 \cdot g^{-1}$)	V_{total} ($cm^3 \cdot g^{-1}$)	V_{mic} ($cm^3 \cdot g^{-1}$)	V_{mes}/V_{total} (%)	V_{ave} (nm)	Density($g \cdot cm^{-3}$)
NFs	10	0.039	0	–	15.7	–
PNF1	22	0.058	0	–	10.4	–
PNF2	53	0.244	0	–	18.5	–
PNF3	66	0.391	0	–	23.7	–
CNFs	638	0.301	0.224	25.5	1.89	0.89
PCNF1	903	0.406	0.307	24.4	1.80	0.84
PCNF2	1006	0.497	0.310	37.6	1.98	0.78
PCNF3	1232	0.786	0.441	43.9	2.55	0.71

The BET specific surface area, pore volume, average pore size, and density of NFs and PNFs are listed in Table 1. Specific surface area and PSD before and after carbonization and activation of the prepared fiber materials follow the same trend with increasing PVP template solvent content. The induced PVP template solvent content decreases under low PVP/PAN proportions (0.2/0.8). In addition, fewer pores with smaller sizes are formed in the nanofiber structure after removal through the hydrothermal process. Compared with NF and CNF prepared through pure PAN-based electro-spinning, the mesopore content and average pore size in PSD are reduced but the BET specific surface area slightly increases. The BET specific surface area, total pore volume, mesoporous rate, and average pore number of the material increase with increasing PVP/PAN proportion. Therefore, the introduction of the PVP template solvent can effectively regulate and control the specific surface area and PSD of nanofibers. PCNF3 exhibits the largest BET specific surface area (1232 $m^2 \cdot g^{-1}$) and the smallest density (0.71 $g \cdot cm^{-3}$), with a mesoporous rate of up to 43.9% and an average pore size of approximately 2.55 nm.

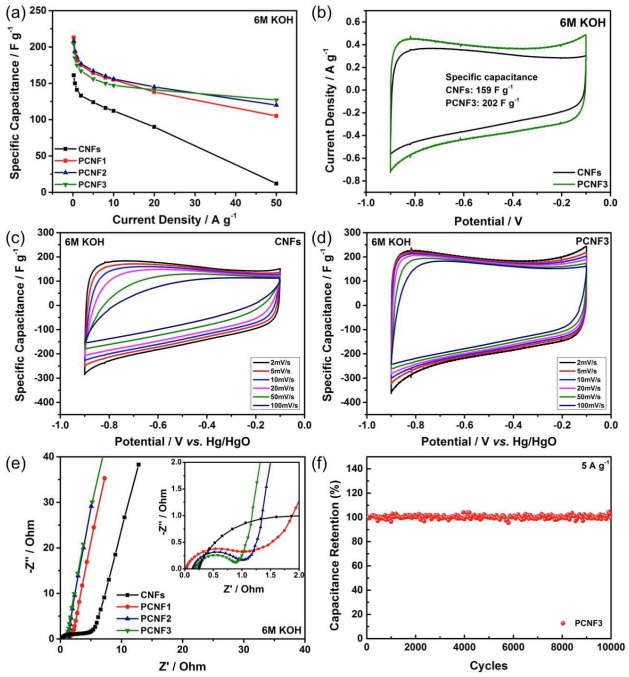

Fig. 7 Electrochemical performance of PCNF compared with CNFs in 6 M KOH electrolyte: (a) specific capacitance *vs*. current density; (b) CV curves of CNFs and PCNF3 at a scan rate of 2 mV·s^{-1}; (c, d) CV curves of CNFs and PCNF3 at the scan rate of 2, 5, 10, 20, 50, and 100 mV·s^{-1}; (e) Nyquist plots from EIS analysis; and (f)cyclic stability of PCNF3 in 10 000 cycles

Fig. 7a shows the change curves of the mass-specific capacitance of CNF and PCNF electrodes versus the current density, which are important parameters for assessing the rate performance of supercapacitor electrode materials. Both CNF and PCNF exhibit good rate performance when the current density is lower than 10 A·g^{-1}, and the capacitance retention rates are more than 70%.The mass-specific capacitance of the CNF electrode rapidly decreases when the current density is further increased. Conversely, the PCNF electrode can still maintain an acceptable capacitance level. Moreover, the mass-specific capacitance of the PCNF3 electrode is retained at approximately 150 F·g^{-1} when the current density is 50 A·g^{-1}. The rate characteristic analysis shows that the PCNF electrode possesses improved electric double-layer capacitance rate than the CNF electrode and can still maintain higher electric double layer capacitance under a large current density; high mesoporous rate enables the smooth access of ions in the electrode pore channel under large current charge and discharge conditions, thereby forming good electric double layer.[33-35]

The CV curves of CNF and PCNF3 electrodes are shown in Figs. 7b–7d. Themass-specific capacitance of the PCNF3 electrode at a scan rate of 2 mV·s^{-1} is 202 F·g^{-1}, whereas the mass-specific capacitance of the CNF electrode is 159 F·g^{-1}, which improves by approximately 27%. Compared with CV curves at scan rates of 2, 5, 10, 20, 50, and 100 mV·s^{-1}, the PCNF3 electrode can maintain improved rectangle degree of the CV curve at a large scan rate. Hence, the PCNF3 electrode exhibits improved rate characteristics than the CNF electrode, which is consistent with the GC test results. Fig. 7e shows the Nyquist plots obtained through EIS analysis. The difference in the equivalent series resistance (ESR) between CNF and PCNF electrodes at the high frequency zone is small. That is, both electrode materials were obtained by carbonizing PAN-based fibers, and the electrical conductivities characterized by the materials are basically the same. The similar linear trend at the low-frequency zone shows that the charge diffusion resistance is identical; hence, the pore spaces of the two electrode materials have similar microporous sizes, and the diffusion efficiency of electrolytes in the pore channels is the same. However, the capacity reactance arc of the PCNF electrode at the middle frequency zone is smaller than that of the CNF electrode. The excellent rate performance of this electrode is mainly attributed to the lower charge transfer resistance. Thus, improvement of mesopores in the nano-scale pore channel of the electrode is beneficial for reducing the charge transfer resistance of the electrode; higher charge efficiency may be brought for the electrode in CDI applications.[36] The PCNF3 electrode exhibits extremely excellent cyclic charge–discharge stability, as determined through analysis of the cyclic stability under a current density of 5 A·g^{-1}; furthermore, 100% of electrode capacitance is retained after 10000 electrode cycles.

Based on material characteristics and electrochemical performance analysis, both the monolithic CNF electrode and high-mesoporous-rate PCNF electrode are regarded as macro-scale two-dimensional monolithic electrode materials with developed pore structures; these electrodes are ideal for CDI. A brand new vertical flow-through CDI module suitable for macro-scale two-dimensional monolithic electrode was designed to determine macro integrity characteristics. Fig. 8a shows the respective curves of conductivity versus the concentration of the monolithic CNF electrode tested by the vertical flow-through and parallel flow-by CDI modules. At the beginning of feeding and before applying voltage, the prepared CNF electrode exhibits a high physical adsorption capacity, such that the developed pore spaces and pore channels of the material confer the material with high adsorption capacity. After applying a voltage of 1.2 V, the current conductivity of the raw feed water rapidly decreases and reaches the balance concentration within 15 min, thereby reaching adsorption saturation. Under the vertical flow-through CDI module, the CNF electrode shows a high CDI adsorption capacity of up to 7.61 mg·g^{-1}, which is 1.87 times higher than the tested capacity (4.07 mg·g^{-1}) of the parallel flow-by CDI module. Fig. 8b shows the curves of current density versus time. Under the vertical flow-through CDI structure, the CNF electrode has a smaller current density at

the initial stage of electric adsorption. The charge efficiency (23.7%) is also improvedby1.51 times compared with that in the parallel flow-by type (15.7%). This change is attributed to the similar developed pore structures of the monolithic CNF electrode to that of macro-scale three-dimensional materials, such as carbon aerogels. When the CNF electrode was used as the CDI electrode, the salt solution is allowed to pass through the pore spaces. Thus, when the CNF electrode was assembled with the vertical flow-through CDI structure, full and rapid contact between the pore spaces of the electrode and the ions in the salt solution is ensured; thus, high CDI adsorption capacity and charge efficiency can be obtained[17].

The prepared highly porous PCNF3 electrode exhibits developed mesopore channels; theoretically, the access of ions to the pore channels is smooth and rapid. Consequently, the resulting comparison with the CNF electrode after the PCHF3 electrode was assembled through the vertical flow-through CDI module is shown in Figs. 8a and 8c. Although the tested adsorption capacity (6.51mg·g^{-1}) of the PCNF3 electrode is lower than that of the CNF electrode (7.61 mg·g^{-1}), the CDI charge efficiency (32.5%) of the PCNF3 electrode is higher than that of the CNF electrode (23.7%). Basing on the analysis results of the powdered active carbon electrode, we concluded that the monolithic CNF electrode, with a mesoporous rate of ~25%, is sufficient to ensure the formation of the CDI adsorption electric double-layer because no adhesives are present to block and damage the effective adsorption pore channel. Moreover, the full contact between the salt solution and the internal part of the electrode are ensured by the developed pore spaces in the vertical flow-through CDI structure. Further improvement of the mesoporous rate will not improve the CDI adsorption capacity. However, similar to the electrochemical performance analysis, high mesoporous rate provides developed nano–scale pore channel distribution for the electrode and improves the transformation and diffusion of ions in the electrode pore channel; therefore, low charge transfer resistance significantly improves the CDI charge efficiency of the electrode and yields higher energy utilization.[37]

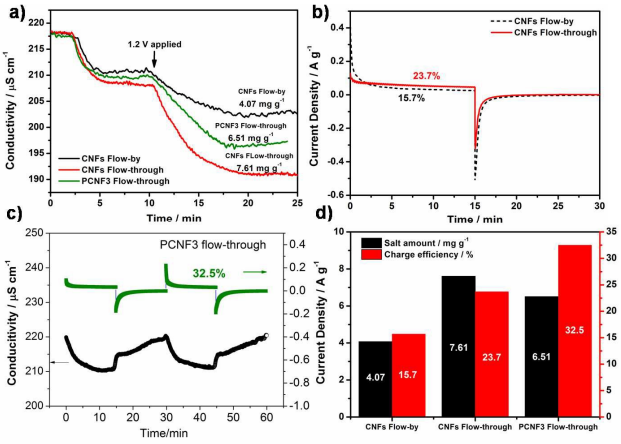

Fig.8 (a) Curves of conductivity versus time; (b) curves of current density versus time; (c) conductivity variation in the effluent and the corresponding current during twocycles; and (d) CDI performance comparison (Testing conditions: 50 mL NaCl solution with an initial concentration of 100 mg·L^{-1} is used; the CDI test is conducted at a feed velocity of 1.5 mL·min^{-1} and an applied voltage of 1.2 V.)

A comprehensive comparison of the CDI test results is shown in Fig. 8d.The designed vertical flow-through CDI structure can greatly improve the adsorption capacity and charge efficiency for the monolithic two-dimensional CNF electrode materials compared with the traditional parallel flow-by CDI structure. Although the adsorption capacity of the prepared high-mesoporous-rate PCNF electrode is not improved in the vertical flow-through CDI structure compared with the CNF electrode, the charge efficiency is higher than that of the CNF electrode and higher CDI energy utilization can be realized.

Conclusions

The as-fabricated CNFs and PCNF electrodes possess macro-scale two-dimensional monolithic structures. The PCNF electrodes have a rough porous fiber surface and increased specific surface area, mesoporous rate, and average pore size with increasing PVP/PAN proportion. The specific surface area of the PCNF3 electrode can reach 1232 m^2·g^{-1},and the mesoporous rate reaches43.9%. The electrochemical test shows that CNF and PCNF electrodes exhibit good electric double-layer capacitance characteristics. The PCNF electrode has excellent electric double-layer characteristics and cyclic stability because of its higher specific surface area and mesoporous rate. The EIS impedance analysis shows that the PCNF electrode has improved charge transfer characteristics than the CNF electrode.

The designed vertical flow-through CDI structure can more accurately illustrate the CDI adsorption performance of the

monolithic CNF electrode; the adsorption capacity reaches 7.61 mg·g^{-1}, and the charge efficiency is 23.7%. The adsorption capacity and the charge efficiency are improvedby1.87 and 1.51 times, respectively, compared with those of the traditional parallel flow-by CDI structure. Although the prepared high-mesoporous-rate PCNF3 electrode has a lower adsorption capacity than the CNF electrode, its charge efficiency is improved to 32.5%, thereby demonstrating its excellent CDI energy utilization.

Acknowledgements

The authors acknowledge the financial support from the National Science Foundation of China (No. 21336001) and the Qaidam Salt Lake Chemical Joint Research Fund Project of NSFC and the State People's Government of Qinghai Province (No. U1507103).

Notes and references

1. S. Porada, R. Zhao, A. van der Wal, V. Presser and P. M. Biesheuvel, *Prog Mater Sci*, 2013, **58**, 1388-1442.
2. C. J. Gabelich, T. D. Tran and S. I. H. Mel, *Environ. Sci. Technol.*, 2002, **36**, 3010-3019.
3. M.-W. Ryoo, J.-H. Kim and G. Seo, *J. Colloid Interface Sci.*, 2003, **264**, 414-419.
4. J.-B. Lee, K.-K. Park, H.-M. Eum and C.-W. Lee, *Desalination*, 2006, **196**, 125-134.
5. P. Xu, J. E. Drewes, D. Heil and G. Wang, *Water Res.*, 2008, **42**, 2605-2617.
6. L. Zou, G. Morris and D. Qi, *Desalination*, 2008, **225**, 329-340.
7. M. A. Anderson, A. L. Cudero and J. Palma, *Electrochim. Acta*, 2010, **55**, 3845-3856.
8. J.-H. Lee, W.-S. Bae and J.-H. Choi, *Desalination*, 2010, **258**, 159-163.
9. M. E. Suss, S. Porada, X. Sun, P. M. Biesheuvel, J. Yoon and V. Presser, *Energ Environ Sci*, 2015, **8**, 2296-2319.
10. G. Wang, Q. Dong, Z. Ling, C. Pan, C. Yu and J. Qiu, *Journal of Materials Chemistry*, 2012, **22**, 21819-21823.
11. Y. Bai, Z. H. Huang, X. L. Yu and F. Y. Kang, *Colloid Surface A*, 2014, **444**, 153-158.
12. X. Wang, J. S. Lee, C. Tsouris, D. W. DePaoli and S. Dai, *Journal of Materials Chemistry*, 2010, **20**, 4602-4608.
13. X. T. Xu, Y. Liu, T. Lu, Z. Sun, D. H. C. Chua and L. K. Pan, *J Mater Chem A*, 2015, **3**, 13418-13425.
14. X. T. Xu, Z. Sun, D. H. C. Chua and L. K. Pan, *Sci Rep-Uk*, 2015, **5**.
15. Y. Liu, L. K. Pan, T. Q. Chen, X. T. Xu, T. Lu, Z. Sun and D. H. C. Chua, *Electrochimica Acta*, 2015, **151**, 489-496.
16. C. L. Yeh, H. C. Hsi, K. C. Li and C. H. Hou, *Desalination*, 2015, **367**, 60-68.
17. M. E. Suss, T. F. Baumann, W. L. Bourcier, C. M. Spadaccini, K. A. Rose, J. G. Santiago and M. Stadermann, *Energ Environ Sci*, 2012, **5**, 9511-9519.
18. S. I. Jeon, H. R. Park, J. G. Yeo, S. Yang, C. H. Cho, M. H. Han and D. K. Kim, *Energ Environ Sci*, 2013, **6**, 1471-1475.
19. K. B. Hatzell, L. Fan, M. Beidaghi, M. Boota, E. Pomerantseva, E. C. Kumbur and Y. Gogotsi, *ACS Appl Mater Interfaces*, 2014, **6**, 8886-8893.
20. M. Wang, Z.-H. Huang, L. Wang, M.-X. Wang, F. Kang and H. Hou, *New Journal of Chemistry*, 2010, **34**, 1843-1845.
21. X. T. Xu, L. K. Pan, Y. Liu, T. Lu and Z. Sun, *Journal Of Colloid And Interface Science*, 2015, **445**, 143-150.
22. C. A. Bonino, L. Ji, Z. Lin, O. Toprakci, X. Zhang and S. A. Khan, *ACS Appl Mater Interfaces*, 2011, **3**, 2534-2542.
23. X. P. Liu, Y. Y. Chen, C. L. Cao, J. Xu, Q. R. Qian, Y. J. Luo, H. Xue, L. R. Xiao, Y. M. Chena and Q. H. Chen, *New Journal Of Chemistry*, 2015, **39**, 6944-6950.
24. M. Wang, Z. H. Huang, L. Wang, M. X. Wang, F. Y. Kang and H. Q. Hou, *New Journal Of Chemistry*, 2010, **34**, 1843-1845.
25. A. F. Che, V. Germain, M. Cretin, D. Cornu, C. Innocent and S. Tingry, *New Journal Of Chemistry*, 2011, **35**, 2848-2853.
26. C. J. Luo, S. D. Stoyanov, E. Stride, E. Pelan and M. Edirisinghe, *Chemical Society reviews*, 2012, **41**, 4708-4735.
27. A. G. El-Deen, N. A. M. Barakat, K. A. Khalil and H. Y. Kim, *J Mater Chem A*, 2013, **1**, 11001-11010.
28. A. G. El-Deen, N. A. M. Barakat, K. A. Khalil and H. Y. Kim, *New Journal Of Chemistry*, 2014, **38**, 198-205.
29. C. Kim, Y. I. Jeong, B. T. N. Ngoc, K. S. Yang, M. Kojima, Y. A. Kim, M. Endo and J. W. Lee, *Small*, 2007, **3**, 91-95.
30. H. J. Pan, J. M. Yang, S. P. Wang, Z. B. Xiong, W. S. Cai and J. Y. Liu, *J Mater Chem A*, 2015, **3**, 13827-13834.
31. Z. Y. Zhang, X. H. Li, C. H. Wang, S. W. Fu, Y. C. Liu and C. L. Shao, *Macromol Mater Eng*, 2009, **294**, 673-678.
32. J. Jagiello and M. Thommes, *Carbon*, 2004, **42**, 1227-1232.
33. R. T. Mayes, C. Tsouris, J. O. Kiggans, Jr., S. M. Mahurin, P. D. W. De and S. Dai, *J. Mater. Chem.*, 2010, **20**, 8674-8678.
34. H. Li, L. Pan, T. Lu, Y. Zhan, C. Nie and Z. Sun, *J. Electroanal. Chem.*, 2011, **653**, 40-44.
35. S. Nadakatti, M. Tendulkar and M. Kadam, *Desalination*, 2011, **268**, 182-188.
36. K. Laxman, L. Al Gharibi and J. Dutta, *Electrochimica Acta*, 2015, **176**, 420-425.
37. Z. Chen, C. Song, X. Sun, H. Guo and G. Zhu, *Desalination*, 2011, **267**, 239-243.

Table of Contents:

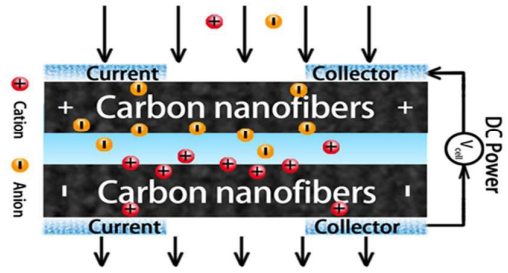

Electrospun carbon nanofibers exhibit enhanced capacitive deionization performance in the vertical flow-through capacitive deionization for desalination.